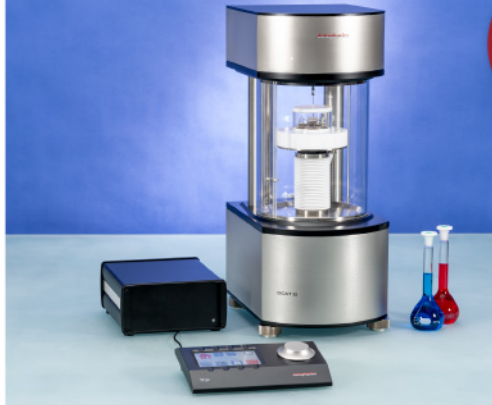




ASTM D5946
ASTM D7334
ASTM D7490
ISO 27448

optical contact angle measurements and drop contour analysis to determine surface energy as well as interfacial and surface tension

force tensiometry, dynamic contact angle measurements, and force of adhesion evaluation



ASTM D1331
ASTM D1417
ISO 1409

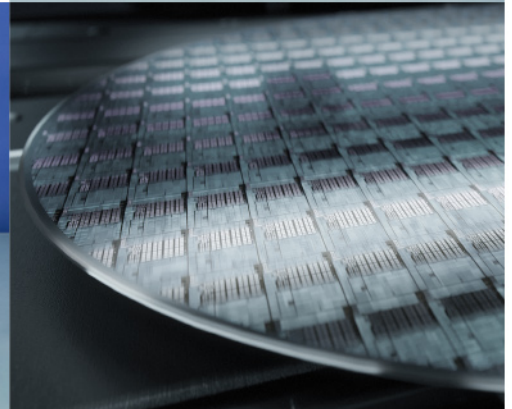


ISO/TR 13097

optical turbidity, stability and aging analysis of multi-phase dispersions



zeta potential measurements of fibres, powders, and plate-shaped solids



High-end, versatile laboratory measurement device portfolio for a comprehensive analysis of surfaces and interfaces

Learn more >

dataphysics
Understanding Interfaces

DataPhysics Instruments GmbH
Raiffeisenstraße 34 • 70794 Filderstadt, Germany
phone +49 (0)711 770556-0 • fax +49 (0)711 770556-99
sales@dataphysics-instruments.com
www.dataphysics-instruments.com

Laminated Organic Photovoltaic Modules for Agrivoltaics and Beyond: An Outdoor Stability Study of All-Polymer and Polymer:Small Molecule Blends

Xabier Rodríguez-Martínez,* Sergi Riera-Galindo, Luis Ever Aguirre, Mariano Campoy-Quiles, Hans Arwin, and Olle Inganäs*

The integration of organic photovoltaic (OPV) modules on greenhouses is an encouraging practice to offset the energy demands of crop growth and provide extra functionality to dedicated farmland. Nevertheless, such OPV devices must meet certain optical and stability requirements to turn net zero energy greenhouse systems a reality. Here a donor:acceptor polymer blend is optimized for its use in laminated devices while matching the optical needs of crops. Optical modeling is performed and a greenhouse figure-of-merit is introduced to benchmark the trade-off between photovoltaic performance and transparency for both chloroplasts and humans. Balanced donor:acceptor ratios result in better-performing and more thermally stable devices than acceptor-enriched counterparts. The optimized polymer blend and state-of-the-art polymer:small-molecule blends are next transferred to 25 cm² laminated modules processed entirely from solution and in ambient conditions. The modules are mounted on a greenhouse as standalone or 4-terminal tandem configurations and their outdoor stability is tracked for months. The study reveals degradation modes undetectable under laboratory conditions such as module delamination, which accounts for 10–20% loss in active area. Among the active layers tested, polymer:fullerene blends are the most stable and position as robust light harvesters in future building-integrated OPV systems.

1. Introduction

A significant fraction of modern plant agriculture occurs in greenhouses, where crops and vegetables can grow with high yields, at fast paces, and with improved quality. Greenhouses might occupy a modest fraction of the mainland of traditional

farming countries. In the case of Spain, greenhouses extend over 77 000 hectares or, equivalently, 0.15% of the total area of the country.^[1] Recent energy balance models suggest that making side use of such surface for electricity generation is an attractive practice toward net zero energy (NZE) greenhouse systems,^[2,3] namely, through semitransparent organic photovoltaics (OPVs) without negatively influencing the crop growth. Early literature has identified greenhouses as a suitable entry market for OPV modules,^[4,5] in which the harvested electricity can be leveraged for ventilating/cooling and lighting to extend the growth period of plants^[3] and reduce the life cycle–CO₂ emissions.^[6] Reports focused on stability performance tracking of OPV modules mounted in greenhouses are, however, scarce.^[7]

The design of agrivoltaic modules demands properties beyond the maximum power conversion efficiency (PCE).^[8,9] In this scenario, optical characteristics such as i) their transparency in the photosynthetically active radiation (PAR) window under incident solar light, also known as crop growth factor (CGF); and ii) their average visible transmittance (AVT), which corresponds to their degree of transparency weighed by the photopic response (PR) of the human eye, are as important as the PCE. Mathematically, the CGF and the AVT are defined as

X. Rodríguez-Martínez, S. Riera-Galindo, O. Inganäs
Biomolecular and Organic Electronics
Department of Physics, Chemistry and Biology
Linköping University
Linköping SE 581 83, Sweden
E-mail: xabier.rodriguez.martinez@liu.se; olle.inganas@liu.se

S. Riera-Galindo, M. Campoy-Quiles
Instituto de Ciencia de Materiales de Barcelona
ICMAB-CSIC, Esfera UAB
Campus Universidad Autónoma de Barcelona
Bellaterra, Barcelona 08193, Spain

L. E. Aguirre
Epishine AB
Wahlbecksgatan 25, Linköping SE 582 13, Sweden
H. Arwin
Materials Optics
Department of Physics, Chemistry and Biology
Linköping University
Linköping SE 581 83, Sweden

 The ORCID identification number(s) for the author(s) of this article can be found under <https://doi.org/10.1002/adfm.202213220>.

© 2022 The Authors. Advanced Functional Materials published by Wiley-VCH GmbH. This is an open access article under the terms of the Creative Commons Attribution License, which permits use, distribution and reproduction in any medium, provided the original work is properly cited.

DOI: 10.1002/adfm.202213220

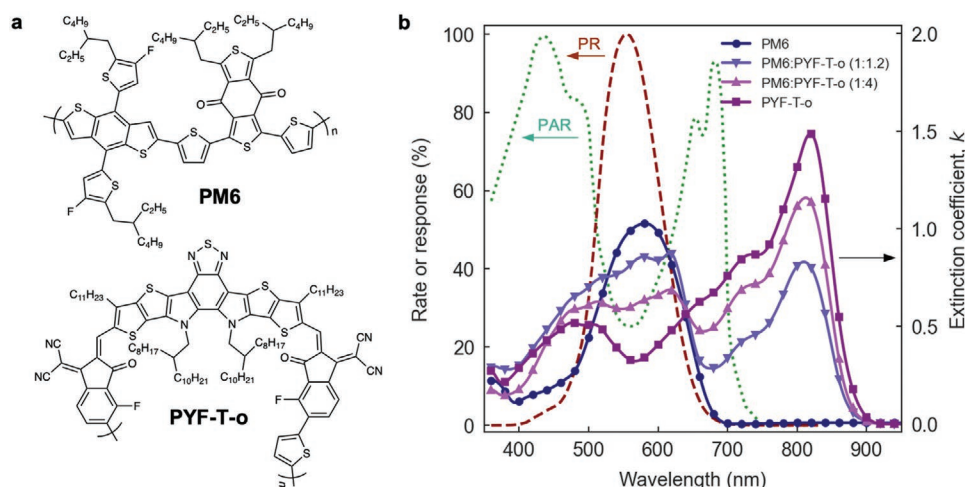


Figure 1. a) Chemical structures of the polymer donor (PM6) and the polymer acceptor (PYF-T-o) used in this work. b) The left axis quantifies either the PAR (dotted green line) or the PR (brown dashed line). The right axis quantifies the k of PM6, PYF-T-o, and two of the blends tested in this work (1:1.2 and 1:4, w:w).

$$CGF = \frac{\int T(\lambda) PAR(\lambda) \Gamma(\lambda) d\lambda}{\int PAR(\lambda) \Gamma(\lambda) d\lambda} \quad (1)$$

and

$$AVT = \frac{\int T(\lambda) PR(\lambda) \Gamma(\lambda) d\lambda}{\int PR(\lambda) \Gamma(\lambda) d\lambda} \quad (2)$$

where λ is the wavelength, $T(\lambda)$ is the transmission of the device under consideration, $PAR(\lambda)$ is the plant action spectrum (PAR in Figure 1b), $PR(\lambda)$ is the photopic response of the human eye (PR in Figure 1b) and $\Gamma(\lambda)$ is the air mass 1.5 global (AM1.5G) solar spectral irradiance, and the integral is taken over this spectrum. On the one hand, a high CGF guarantees that solar power generation does not compete excessively with the optical requirements of photosynthesis. Several factors affect crop growth or production, including internal factors (like genetic or heredity) and external factors (environmental), such as climatic, edaphic, biotic, physiographic, and socioeconomic. The calculation of the CGF could be accordingly adapted, e.g., by selecting an appropriate PAR spectrum to mimetic some of those factors or target crops. However, this goes beyond the scope of the present work and the absorption spectrum of an isolated chloroplast (PAR in Figure 1b) is considered as a convoluted general case of the action spectra of chlorophyll A, chlorophyll B, and most carotenoids (Figure S1, Supporting Information). A CGF between 10–50% is typically required for agricultural purposes.^[8] On the other hand, a high AVT assures that routine maintenance activities inside the greenhouse can be performed in absence of indoor lighting (similarly to windows),^[10] as well as meeting certain aesthetic requirements.^[11] However, an excessively high AVT might negatively influence the photosynthetic mechanism of plants due to increased temperature. Therefore, PV modules optimized for greenhouses should provide a golden mean of all three features: PCE, CGF, and AVT.

OPVs are particularly suitable for their deployment onto greenhouses. The optical properties of the organic photoactive

materials, such as the optical band gap, can be tuned via chemical and structural modifications, thus offering a plethora of adjustments on the CGF and the AVT. Using OPV, a maximum PCE of $\approx 17\%$ has been theoretically predicted based on the assumptions of the Shockley–Queisser limit and the additional condition of avoiding absorption in the visible part of the solar spectrum.^[5] Non-fullerene acceptors (NFAs) acting as near-infrared absorbers represent the current state-of-the-art acceptor molecules in high-performing OPV devices.^[12] The workhorse NFA 2,2'-(2Z,2'Z)-((12,13-bis(2-ethylhexyl)-3,9-diundecyl-12,13-dihydro-[1,2,5]thiadiazolo[3,4-e]thieno[2'',3''':4',5'']thieno[2'',3'':4,5]pyrrolo[3,2-g]thieno[2'',3'':4,5]thieno[3,2-b]indole-2,10-diyl)bis(methanylylidene))bis(5,6-difluoro-3-oxo-2,3-dihydro-1H-indene-2,1-diylidene))dimalononitrile (Y6) in combination with donor polymers such as poly[[4,8-bis[5-(2-ethylhexyl)-4-fluoro-2-thienyl]benzo[1,2-b:4,5-b']dithiophene-2,6-diyl]-2,5-thiophenediyl[5,7-bis(2-ethylhexyl)-4,8-dioxo-4H,8H-benzo[1,2-c:4,5-c']dithiophene-1,3-diyl]-2,5-thiophenediyl] (PM6, Figure 1a) broadly exceeds 15% PCE in laboratory scale and on opaque devices,^[13] with recent records of 17.3% in binary single-junctions for optimized device configurations and processing conditions.^[14] Semitransparency reduces photocurrents and PCE, hence more sophisticated polymer:NFA:fullerene blends have been proposed to maintain high performance and meet the needs of greenhouses.^[15] Interestingly, the (co-)polymerization using Y6 as the main repeating unit with different linkers (such as thiophenes, vinylenes, 2,2'-bithiophenes or thieno[3,2-b]thiophenes)^[16–18] is receiving attention as the corresponding polymers maintain comparable PCE, optical and transport properties while offering the intrinsic processability advantages ascribed to macromolecules. These are especially acknowledged when blended with analog donor polymers to form all-polymer OPV blends, which show excellent morphological stability and mechanical flexibility.^[17] One of the most successful polymerizations of Y-family molecules reported so far is the so-called PYF-T-o variant^[17] (Figure 1a) showing a record PCE of 17.06%.^[19] This polymer maintains a low band gap, featuring an absorption onset at 850 nm that barely disturbs the optical needs

of plants and humans (Figure 1b). On the other hand, dilute donor OPV devices are also interesting from an agrivoltaic perspective to improve the required CGF and AVT.^[20] Recently, highly unbalanced PM6:Y6 (1:4, w:w) blends were reported to show competitive PCEs of 7.46% under 1 sun with an AVT of 36.4%,^[21] which encourages the use of similarly highly diluted donor blends in all-polymer OPV devices.

In this work, we first combine donor and acceptor polymers in a photoactive blend that matches the needs of agrivoltaic devices, i.e., CGF and AVT both above the 30% threshold. Device prototyping occurs mostly by lamination in air,^[22,23] a roll-to-roll (R2R) compatible method in which two separate device stacks are glued together at their photoactive layer (PAL) to render functionality.^[24] PALs are deposited by blade coating, using slot-die coated PEDOT(PSS) layers as electrodes with an electron transport layer (ETL) added on the cathode side. These films are supported on flexible polyethylene terephthalate (PET) foil substrates and the devices are completed by lamination at their PALs. All-polymer blends are screened in two different exemplary ratios and benchmarked according to a new figure-of-merit that weighs the transparency and performance needs of agrivoltaics: the greenhouse figure-of-merit (gh-FoM). In terms of thermal stability, a balanced donor:acceptor ratio (1:1.2, w:w) is found to outperform the unbalanced counterpart (1:4) despite its lower gh-FoM. To demonstrate scalability, we prototype 25 cm² minimodules of selected blends following proprietary methods of Epishine AB. All-polymer blends together with further PAL systems (NFA- and fullerene-based bulk heterojunctions) are characterized in simulated indoor lighting before being deployed in real outdoor testing conditions, i.e., in a domestic greenhouse under natural illumination. We design a low-cost and autonomous *I-V* tracing system that uploads the corresponding PV figures of merit wirelessly to the cloud. Our outdoor testing protocol in a greenhouse complies with the ISOS-O-2 standard^[25,26] and it reveals further degradation modes, such as delamination, derived from aggressive thermal and humidity cycles registered over a period of up to 58 days. Notably, these failure modes are omnipresent in all PALs and device configurations tested outdoors while absent in standard laboratory testing conditions. Our observations highlight the importance of performing stability studies under real operating environments. Among the PALs tested and modules fabricated complying with R2R requirements, fullerene-based counterparts are the most stable and attractive from a building-integrated OPVs industrial perspective.

2. Results and Discussion

2.1. Modeling and Screening of Polymer Blends in Laminated Device Structures

The structures of the polymer donor (PM6) and the polymer acceptor (PYF-T-o) considered in this work are shown in Figure 1a. As per its ellipsometrically deduced extinction coefficient (*k*), PM6 shows its main absorption band (centered at ≈580 nm) well-aligned with the minimum of the PAR action spectrum of an isolated chloroplast (at ≈565 nm), thus matching the needs of crops growth (Figure 1b). Since the

absorption spectrum of PM6 mostly overlaps the PR, a trade-off will arise between CGF and AVT influenced by the polymer donor content in the blend. On the other hand, the main absorption band of PYF-T-o is significantly red-shifted, so it barely competes with crops. Its *k* shows a local minimum precisely where the PAR spectrum does, and the PR reaches its absolute maximum. Notably, the *k* of neat PYF-T-o is among the highest ever reported for π -conjugated polymers,^[27,28] with its value peaking close to 1.5 (1.48) at 820 nm (values that are very similar to those observed on neat Y6 films).^[28] This fact enables PYF-T-o-based blends to be made thin (<100 nm) while keeping excellent light-harvesting capabilities, which could also be a positive strategy to improve thermal stability.^[29] Thus, from an optical point of view, PYF-T-o is certainly an ideal polymer acceptor for agrivoltaics.

The device stack used in the optical simulations is detailed in Figure 2a. The three key magnitudes to be optimized in OPV modules for their integration onto greenhouses (PCE, CGF, and AVT) cannot be screened straightaway. Particularly, the PCE is a derived magnitude that should either include electrical and device modeling considerations, or multiple device assumptions (such as in Scharber's model).^[30] Nevertheless, the upper limit to the short-circuit current density (J_{sc}) can be calculated solely by optical models^[31] initially considering 100% internal quantum efficiency (IQE) of exciton-to-charge generation. Moreover, the J_{sc} should be a reasonable proxy of the PCE given their proportionality relation verified in experiments^[32,33] and large databases.^[34] Despite its limitations, J_{sc} is the main PV performance metric that we compute in this work. In our simulations, the PAL is screened in terms of thickness (*t*) and donor:acceptor ratio (ϕ); the remaining layers have their thickness fixed, and we consider incoherent transmission through both the PET substrate and the PET superstrate, leading to a semitransparent device as seen by the chloroplasts (CGF) and the human eye (AVT). The corresponding metrics, namely J_{sc} (Figure 2b), CGF (Figure 2c), and AVT (Figure 2d), are calculated within a range of *t* values of interest for greenhouses ranging from 25 to 125 nm. The corresponding color (in transmission) is also detailed in Figure S2, Supporting Information. On the other hand, ϕ is assumed to govern the optical properties of the PAL following Bruggeman's effective medium approximation^[35] in which the measured refractive indices of the neat materials (Figure 1b) are used as model inputs.

As expected for semitransparent devices, J_{sc} increases steadily with *t* in PM6:PYF-T-o blends (Figure 2b). The effect is more pronounced as the PAL becomes acceptor-enriched due to the broader absorption features and lower band gap of PYF-T-o, which better match the higher photon flux in the near-infrared window of the AM1.5G solar irradiance spectrum. Therefore, acceptor-enriched blends could a priori lead to higher photocurrents. Contrarily, the CGF (Figure 2c) decays rather linearly with *t*. For a given *t*, we observe that donor-enriched blends enable higher CGF, which certainly could be positive for plant growth yet limiting the light-harvesting performance (Figure 2b). Interestingly, a CGF comprised between 20–50% is achievable by almost any blend provided *t* stays in the 50–100 nm regime. Beyond those *t* values, the CGF might be too low (<20%) to guarantee proper plant growth. Finally, the AVT (Figure 2d) shows a mirrored dependence with respect to

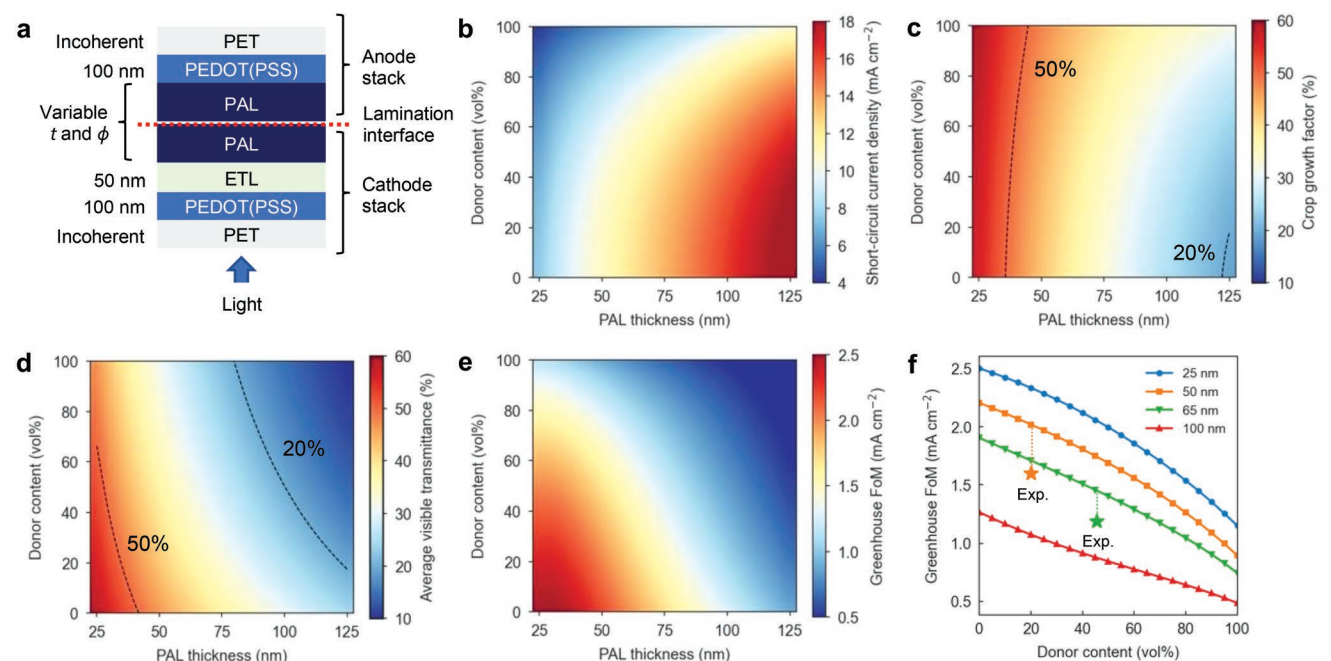


Figure 2. a) Laminated device stack used in the optical simulations with PM6:PYF-T-o as PAL. b) J_{sc} , c) CGF with contours at 50% and 20%, d) AVT with contours at 50% and 20%, and e) the gh-FoM as a function of t (x-axis) and ϕ (y-axis). f) Line cuts of the gh-FoM as a function of ϕ for four different t values. Comparative experimental data is also included for $t = 50$ nm and $\phi = 20$ vol% (orange star), and $t = 65$ nm and $\phi = 45$ vol% (green star).

the CGF (Figure 2c), i.e., donor-enriched PALs are more opaque for the human eye and their AVT varies between 20–50% for t values comprised between 50–100 nm. Certainly, a specific metric is needed to evaluate how PV performance, plant growth, and visible transmittance could be properly adjusted in greenhouses and benchmark different PALs and device structures. For that purpose, we introduce a gh-FoM calculated as

$$\text{gh-FoM} = J_{sc} \times \text{CGF} \times \text{AVT} \quad (3)$$

which has the same units as J_{sc} . In our first approximation, we consider equal weights (or prefactors) for all three involved magnitudes ($J_{sc}:\text{CGF}:\text{AVT}$, 1:1:1). However, as the PV efficiency might be influenced by the greenhouse location and orientation (latitude, incident angle), the specific CGF of the targets, or the importance that plant growth might have compared to power generation,^[2] prefactors might be subject to change. Figure 2e shows the gh-FoM for the PM6:PYF-T-o case, in which acceptor-enriched blends show potentially superior performance if installed on a greenhouse. Line cuts of the gh-FoM at given t values (Figure 2f) are used to benchmark different PALs (Figure S3, Supporting Information). These indicate that the thinner the PAL and the lower the donor polymer volume fraction, the higher the corresponding gh-FoM. Such a rule of thumb applies provided fullerenes are not the main acceptor component of the blend, in which case balanced donor:acceptor ratios offer superior performance (Figure S3, Supporting Information). For comparative purposes, Figure 2f includes two experimental data points obtained in this work (see below). Despite the gh-FoM mismatch, the overall qualitative trends still hold, and they perfectly agree when considering an IQE of 80% in the optical simulations (Figure S4, Supporting Information).

Therefore, thin PALs and acceptor-enriched blends constitute our first experimental candidates for high-performing, greenhouse-integrated OPV devices.

The device structure initially employed in our experimental study is that shown in Figure 2a, i.e., proof-of-concept devices prepared by lamination, where poly(3,4-ethylenedioxythiophene)(poly(styrenesulfonate)) (PEDOT(PSS)) is used as semi-transparent electrode. Note that these devices are initially optimized for indoor operation, as the sheet resistance of thin (100 nm) PEDOT(PSS) contacts ($\approx 150 \Omega \text{ sq}^{-1}$) adds excessive losses on the corresponding J - V curves under 1 sun (Figure S5, Supporting Information). However, studying laminated devices based on PEDOT(PSS) offers several advantages such as cheaper and faster device prototyping compared to indium tin oxide (ITO)-rich devices with thermal evaporated contacts, preserving an architecture that is fully compatible with R2R up-scaling and greenhouse integration. Indoor PV performance will also suffice to understand the PAL processing limitations (if any) and serve as testing bench of other relevant device features such as thermal stability, which is particularly relevant in greenhouse applications.

We start our experiments by exploring the PV performance and optical properties of unbalanced PM6:PYF-T-o ratios, which yielded encouraging results in analogous PM6:NFA blends (e.g., PM6:Y6).^[21] The results presented in **Table 1** and **Figure 3a** correspond to PM6:PYF-T-o 1:4 (w:w) blends processed by either spin coating or blade coating. These samples are characterized under indoor illumination (500 lux or $\approx 150 \mu\text{W cm}^{-2}$, Figure S6, Supporting Information) and upon different illumination sides (cathode or anode sides, corresponding to solid and dashed lines, respectively, in Figure 3). However, for benchmarking purposes we have also performed

Table 1. PV figures-of-merit upon illumination side of laminated PM6:PYF-T-o (1:4, w:w) devices under 500 lux; and optimum performance of opaque, inverted blade coated devices with thermally-evaporated back contacts, as characterized under simulated 1 sun conditions.

PAL processing method	Illumination side	V_{oc} [V]	J_{sc} [$\mu\text{A cm}^{-2}$]	$J_{EQE, LED}$ [$\mu\text{A cm}^{-2}$]	FF [%]	PCE [%]	AVT [%]	LUE [%]	$J_{EQE, sun}$ [mA cm^{-2}]	CGF [%]	gh-FoM [mA cm^{-2}]
Spin coating in N_2	Cathode	0.61	21.0	–	54.5	4.6	–	–	–	–	–
	Anode	0.61	20.9	–	57.6	4.9	–	–	–	–	–
Spin coating in air	Cathode	0.64	21.4	–	57.3	5.2	–	–	–	–	–
	Anode	0.63	20.3	–	55.2	4.7	–	–	–	–	–
Blade coating in air (thick)	Cathode	0.65	21.8	22.3	64.8	6.2	35.5	2.2	10.4	35.8	1.32
	Anode	0.65	20.8	20.7	61.7	5.5	–	2.0	9.8	–	1.25
Blade coating in air (thin)	Cathode	0.62	14.9	17.1	66.2	4.1	44.5	1.8	8.1	44.5	1.60
	Anode	0.62	14.2	14.9	66.1	3.9	–	1.7	7.3	–	1.45
Blade coating in N_2	Inverted, opaque	0.89	12.3 mA cm^{-2}	–	58.1	6.4	–	–	–	–	–

a high-throughput screening study to optimize the performance of opaque, inverted blade coated devices, featuring thermally evaporated contacts and characterized under simulated 1 sun conditions (Figure S7, Supporting Information). In PM6:PYF-T-o 1:4 blends, the champion J - V curve (black solid line in Figure 3a) returned an open-circuit voltage (V_{oc}) of 0.89 V, a J_{sc} of 12.3 mA cm^{-2} , a fill factor (FF) of 58.1% and a modest PCE of 6.4%, in line with previous results in diluted donor blends.^[20,21]

We observe that the resulting indoor PCE (Table 1) does not critically depend on the illumination side: the PCE gap between cathode and anode sides is always below 15% (relative) of the highest PCE. This constitutes an important advantage of polymer blends with respect to other donor:acceptor combinations such as polymer:fullerene, which report a severe asymmetric photocurrent extraction upon air processing.^[22] We observe that the cathode side PCE ($\text{PCE}_{\text{cathode}}$) slightly

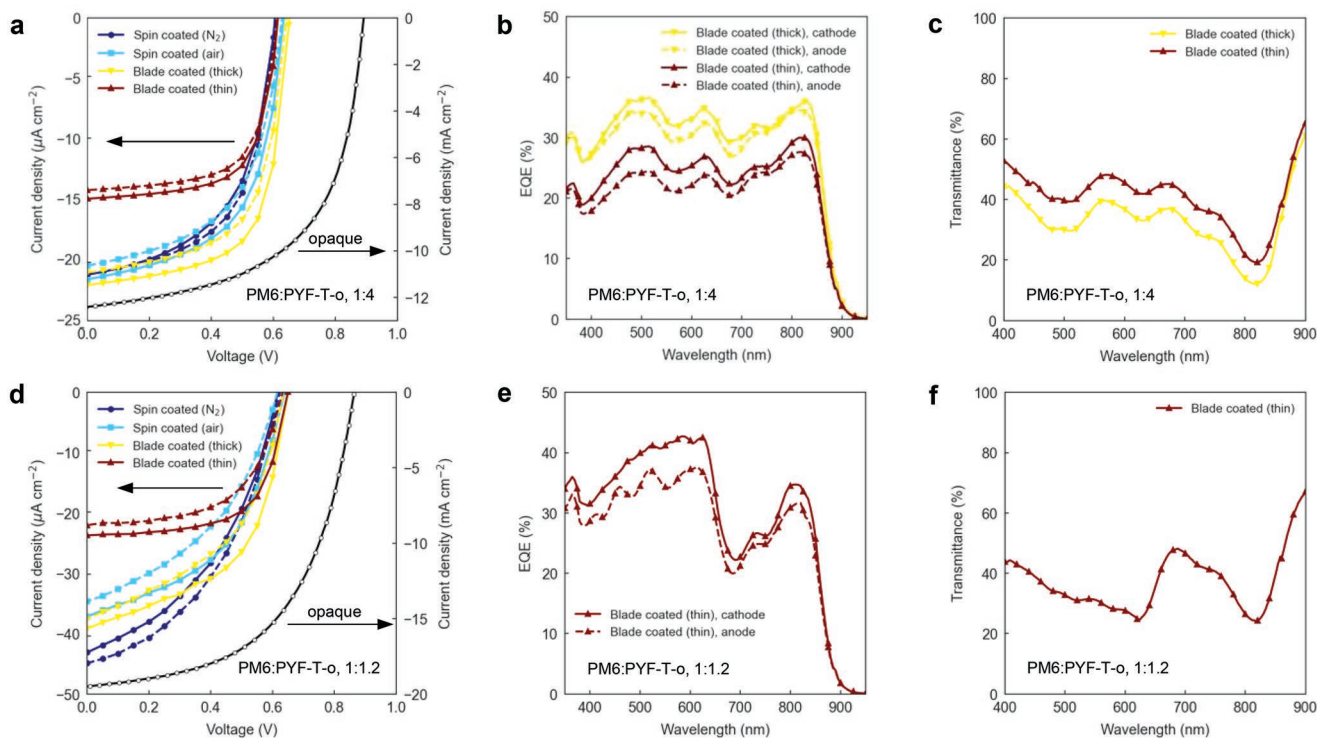


Figure 3. a) J - V curves under 500 lux for laminated PM6:PYF-T-o (1:4, w:w) devices (left axis) and under 1 sun conditions for blade coated devices featuring ITO and evaporated back contacts (right axis). b) EQE spectra of blade coated laminated devices (1:4) upon cathode and anode side illumination. c) Transmittance of the laminated blade coated devices (1:4). d) J - V curves under 500 lux for laminated PM6:PYF-T-o (1:1.2, w:w) devices (left axis) and under 1 sun conditions for blade coated devices featuring ITO and evaporated back contacts (right axis). e) EQE spectra of a blade coated laminated device (1:1.2) upon cathode and anode side illumination. f) Transmittance of the laminated blade coated device (1:1.2).

outperforms the anode side PCE (PCE_{anode}) when the PAL is processed in air (similarly to other reports).^[22] The trend inverts ($PCE_{\text{anode}} > PCE_{\text{cathode}}$) only when the PAL is processed in an inert atmosphere at the expense of lower V_{oc} (0.61 V versus 0.63–0.64 V). Blade coated devices in air can equally maintain excellent performance, with the V_{oc} found to increase further (0.65 V) together with the FF (exceeding 60%). As a result, comparatively thick (>100 nm) blade coated devices show better PCE (6.2% and 5.5% for cathode and anode sides, respectively) than the spin coated counterparts (5.2% and 4.7% for cathode and anode sides, respectively). By preparing thinner blade coated devices (≈ 26 nm per PAL, see Figure S8a, Supporting Information), the FF exceeds 66% at the expense of lower V_{oc} (0.62 V) and J_{sc} (14.9 and 14.2 $\mu\text{A cm}^{-2}$ for cathode and anode sides, respectively) while keeping decent PCE values (4.1% and 3.9% for cathode and anode sides, respectively). Reassuringly, the device performance is very well maintained in the transition from inert to air conditions and shows excellent compatibility with blade coating, which are especially acknowledged features in their potential industrialization. Upon integration of the external quantum efficiency (EQE) spectra (Figure 3b) we find reasonably good agreement with the J - V curves indoors (c.f. J_{sc} and $J_{\text{EQE, LED}}$, Table 1). Weighting the EQE integration by the AM1.5G irradiance spectrum allows estimating the corresponding J_{EQE} under 1 sun ($J_{\text{EQE, sun}}$, Table 1). From the corresponding transmission spectra (Figure 3c), we calculate the AVT, the light utilization efficiency (LUE, here defined as the product of indoor PCE and AVT),^[36] and the CGF (Table 1). The resulting gh-FoM for sun conditions is detailed in Table 1, where it becomes evident the larger potential and suitability of thinner devices to meet the integration requirements of greenhouses.

Thermal stability tests are performed by introducing the laminated devices in an oven at 70 °C, while in a nitrogen-filled glovebox and in the dark. The J - V curves of the blade coated (thin) device as illuminated from its cathode and anode sides are shown in Figure S9, Supporting Information, which indicates that over a period of 30 days the main performance losses are attributed to the V_{oc} and the FF. The resulting T_{80} values

(calculated as the time required to drop the PCE to 80% of its initial value) read 44 and 49 h for cathode and anode side illumination conditions, respectively (Figure S9c, Supporting Information). In parallel, a thermal stability study performed on the spin coated device reveals a similar T_{80} for the cathode side (39 h) yet a significantly enhanced T_{80} for anode side illumination conditions (160 h, Figure S10, Supporting Information). Such dichotomy between blade and spin coated devices suggests that the PAL does not acquire equivalent morphologies on the anode side, which in turn could be more sensitive than initially expected upon processing conditions. In spite of their superior gh-FoM values, unbalanced PM6:PYF-T-o blends might not offer adequate thermal stability for their successful implementation onto greenhouses.

We proceed by investigating the PV performance of laminated PM6:PYF-T-o blends in a 1:1.2 (w:w) ratio, which agrees with the previously reported optimized composition (in terms of PCE).^[17] In this regard, we have verified that substituting chloroform with *o*-xylene as the main solvent does not introduce severe losses of device performance (Figure S11, Supporting Information), which is a positive finding to remove as many chlorinated (co)-solvents as possible from the device manufacture. The high-throughput optimization of benchmark (opaque) inverted blade coated devices (Figure S12, Supporting Information) yields the optimized J - V curve shown in Figure 3d as a black solid line, featuring a V_{oc} of 0.86 V, a J_{sc} of 19.5 mA cm^{-2} , a FF of 54.7% and a PCE of 9.2% under 1 sun. Notably, this implies a 44% increase of the PCE (mainly driven by the J_{sc}) with respect to the unbalanced (1:4) polymer ratio. Regarding semitransparent laminated devices and by employing analogous processing conditions, we observe a few similar performance trends as those using the unbalanced PM6:PYF-T-o ratio (Table 2). For instance, we notice that $PCE_{\text{anode}} < PCE_{\text{cathode}}$ in all scenarios except under an inert atmosphere, in which case the trend also inverts ($PCE_{\text{anode}} > PCE_{\text{cathode}}$) and V_{oc} stays up to 20 mV below the values attained in air. However, in the transition from spin coating in an inert environment to air, J_{sc} suffers a $\approx 15\%$ loss on its cathode side (from 42.6 to 36.8 $\mu\text{A cm}^{-2}$) and $\approx 25\%$ (from 44.4 to 34.4 $\mu\text{A cm}^{-2}$) on its anode side. The

Table 2. PV figures-of-merit upon illumination side of laminated PM6:PYF-T-o (1:1.2, w:w) devices under 500 lux; and optimum performance of opaque, inverted blade coated devices (1:1, w:w) with thermally-evaporated back contacts, as characterized under simulated 1 sun conditions.

PAL processing method	Illumination side	V_{oc} [V]	J_{sc} [$\mu\text{A cm}^{-2}$]	$J_{\text{EQE, LED}}$ [$\mu\text{A cm}^{-2}$]	FF [%]	PCE [%]	AVT [%]	LUE [%]	$J_{\text{EQE, sun}}$ [mA cm^{-2}]	CGF [%]	gh-FoM [mA cm^{-2}]
Spin coating in N_2	Cathode	0.62	42.6	–	42.7	7.5	–	–	–	–	–
	Anode	0.63	44.4	–	43.7	8.1	–	–	–	–	–
Spin coating in air	Cathode	0.64	36.8	–	48.0	7.6	–	–	–	–	–
	Anode	0.62	34.4	–	42.1	6.0	–	–	–	–	–
Blade coating in air (thick)	Cathode	0.65	38.8	–	52.3	8.8	–	–	–	–	–
	Anode	0.64	37.3	–	47.1	7.5	–	–	–	–	–
Blade coating in air (thin)	Cathode	0.65	23.8	26.2	64.1	6.6	30.2	2.0	10.6	37.1	1.19
	Anode	0.64	22.1	22.9	57.9	5.4	–	1.6	9.5	–	1.06
Blade coating in N_2 (1:1)	Inverted, opaque	0.86	19.5 mA cm^{-2}	–	54.7	9.2	–	–	–	–	–

increase in V_{oc} and FF observed in air serve to hold a comparable $PCE_{cathode}$ (7.5% and 7.6% in nitrogen and in air, respectively) yet significantly decreasing PCE_{anode} (from 8.1% to 6.0% in nitrogen and in air, respectively). As a result, the PCE gap between cathode and anode sides is now higher, even exceeding 25% (relative) in some cases (e.g., by spin coating in air). This is indicative that a higher loading of PM6 in the blends might compromise their air-processability in laminated architectures.

Blade coated devices in air demonstrate improved performance with respect to spin coated ones (even when in the glovebox), which constitutes an encouraging finding. Blade coating of thick (>100 nm) devices result in higher V_{oc} values, reading 0.65 V and 0.64 V for the cathode and anode sides, respectively. Moreover, the J_{sc} values appear highly symmetric (38.8 and 37.3 $\mu A\ cm^{-2}$ for cathode and anode, respectively) which in addition to the moderate FF values (52.3% and 47.1% for cathode and anode, respectively) eventually allow $PCE_{cathode} = 8.8\%$ and $PCE_{anode} = 7.5\%$ (indoors). By making blade coated devices thinner ($\approx 32\ nm$ per PAL, see Figure S8b, Supporting Information), V_{oc} is observed to remain invariant, J_{sc} decreases (23.8 and 22.1 $mA\ cm^{-2}$ for cathode and anode, respectively), and FF reaches 64.1% (cathode) and 57.9% (anode). As a result, indoor $PCE_{cathode} = 6.6\%$ and $PCE_{anode} = 5.4\%$. Upon integration of the corresponding EQE (Figure 3e) $J_{EQE, LED}$ confirms good matching with the J_{sc} values extracted from the $J-V$ curves (Table 2). Transmission spectra (Figure 3f) indicate an AVT and a CGF of 30.2% and 37.1%, respectively, for blade coated devices; as expected, these values are below those previously obtained using the PM6:PYF-T-o 1:4 ratio (44.5%) due to the higher PM6 loading. However, the LUE (indoors) is comparable to that observed in unbalanced devices reaching 2.0% (cathode) and 1.6% (anode) precisely due to the higher PM6 loading, which increases the spectral matching with the indoor LED source (Figure S6, Supporting Information). By calculating $J_{EQE, sun}$, we estimate the corresponding gh-FoM to be between 1.19 and 1.06 for the cathode and anode sides, respectively, which are certainly below those obtained for 1:4 PM6:PYF-T-o devices (c.f. Table 1).

The outcomes of the thermal stability tests indicate T_{80} values (Figure S13c, Supporting Information) reading 218 and 345 h for the cathode and anode sides, respectively, which imply an improvement of 500% and 700% with respect to acceptor-enriched ratios. Notably, the main performance losses are attributed to V_{oc} and FF as J_{sc} remains strikingly stable (Figure S13d, Supporting Information). The FF values are observed to increase up to 65.0% after 24 h of thermal stress (Figure S13d, Supporting Information), which helps to significantly increase the PCE and reduce the cathode/anode asymmetry to <10%. The thermal stability accordingly improves, yet the origin of such a positive effect is unknown. We hypothesize that thermal annealing after complete device lamination should be considered in upcoming optimization protocols due to its potentially positive effect on device performance, e.g., by improving the continuity of the bulk heterojunction at the lamination interface and facilitating charge transport. In summary, Figure 4 aggregates the thermal stability data collected for laminated devices in this work, which evidences that despite offering a worse performance-to-transparency ratio (as quantified by their gh-FoM), blade coated 1:1.2 PM6:PYF-T-o blends

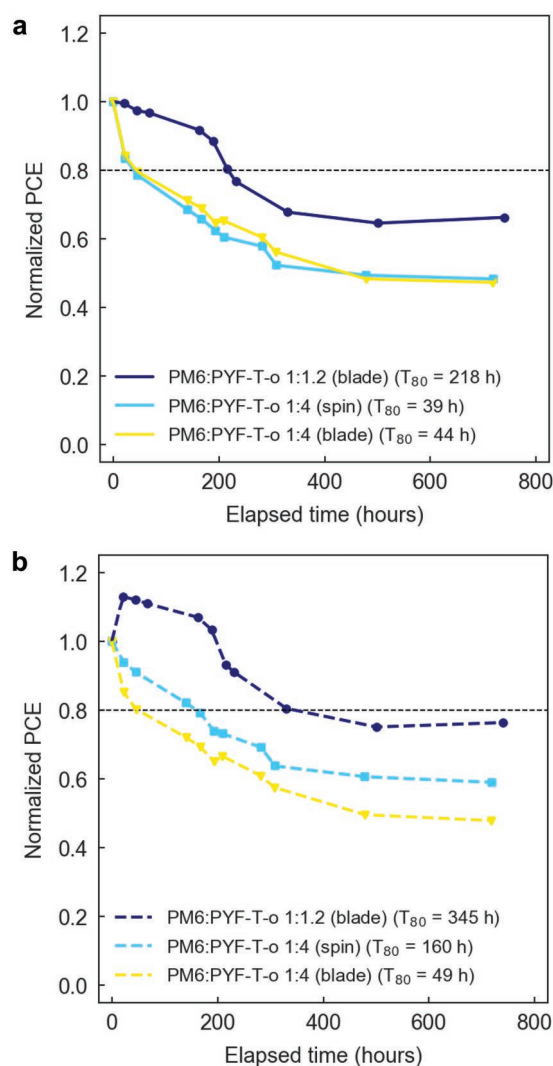


Figure 4. Stability data for laminated devices plotted as the normalized PCE as a function of thermal stress time (70 °C in nitrogen and in the dark). a) Data for cathode side illumination. b) Data for anode side illumination. The dotted lines correspond to the 80% stability threshold used to determine T_{80} .

are far superior in terms of thermal stability in laboratory assays.

2.2. Field-Testing of Laminated PV Modules on a Greenhouse

Assessing the stability of agrivoltaic PV modules while mounted on a greenhouse is necessary to reproduce the harsher environmental conditions (daylight, humidity, temperature) expected therein and identify more realistic device pitfalls, which can be barely reproduced in standard laboratories.^[25] In this section, we prototype, deploy, and perform (greenhouse) outdoor tracking under the ISOS-O-2 standard^[26] of laminated OPV modules. Our objective is to evaluate how the performance losses occur and to identify the main degradation mechanisms and stressors found in greenhouse environments, under real-world testing conditions.

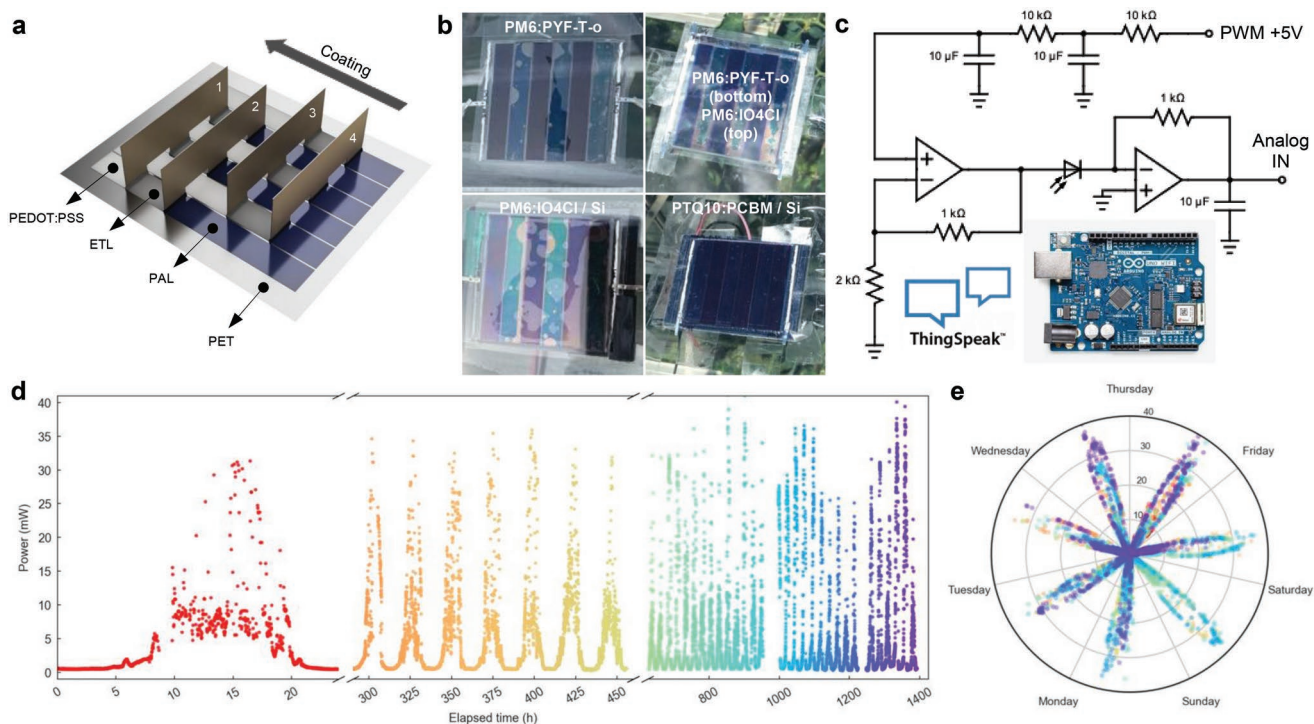


Figure 5. a) 6-cell module prototyping performed by blade coating the ETL and PAL on slot-die-coated PEDOT(PSS) stripes. Laser-cut shims of adequate pitch are sequentially employed to guide film patterning. b) Photographs of four different module configurations as installed on the greenhouse: 2-terminal PM6:PYF-T-o module (top left); 4-terminal tandem with PM6:PYF-T-o as a bottom module and PM6:IO4Cl as a top module (top right); and 4-terminal OPV/Si tandems using PM6:IO4Cl (bottom left) or PTQ10:PCBM (bottom right) as photoactive materials. c) Electronic circuit diagram of the I - V tracer used in combination with an Arduino UNO WiFi Rev2 and the ThingSpeak™ platform. d) Exemplary P trend of a commercial silicon minimodule over a period of 1400 h while on the greenhouse. Color varies from red to purple linearly with the elapsed time. e) Weekly polar plot of that same P data. Note that color coding is preserved and data points are mostly overlapped, thus suggesting excellent stability of the silicon minimodule.

The 25 cm² modules feature 6 cells connected in series following Epishine AB's proprietary technology. On laboratory scale, module manufacturing requires patterning of the ETL and PAL by adapting a laser-cut shim of adequate pitch to a blade applicator, followed by a sequential coating of the layers (Figure 5a). In addition to the previously optimized all-polymer blend including PM6:PYF-T-o (1:1.2, w:w) as PAL (Figure 5b, top left), the outdoor stability study includes additional device structures and PAL materials (Figure S14, Supporting Information) to gain further insights about degradation dynamics in laminated OPV modules for agrivoltaics. More precisely, we set up 4-terminal OPV tandems where PM6:PYF-T-o is used as bottom module PAL and PM6:3,9-bis[5,6-dichloro-1*H*-indene-1,3(2*H*)dione]-5,5,11,11-tetrakis(4-hexylphenyl)-dithieno[2,3-*d*:2',3'-*d'*]-s-indaceno[1,2-*b*:5,6-*b'*]dithiophene (IO4Cl) as top module PAL (Figure 5b, top right); and two organic/inorganic tandem structures including either PM6:IO4Cl (Figure 5b, bottom left) or the recently optimized poly[(thiophene)-*alt*-(6,7-difluoro-2-(2-hexyldecyloxy)quinoxaline)]:[6,6]-phenyl-C₆₁-butyric acid methyl ester (PTQ10:PCBM) blend^[23] (Figure 5b, bottom right) as top modules, in combination with an opaque silicon minimodule underneath (bottom module). PM6:IO4Cl is an NFA-based, high band gap PAL material combination that was originally formulated for indoor applications^[37] yet used here to complement the red-shifted absorption profile of the PM6:PYF-T-o blend and realize "black" tandems. On the other hand,

PTQ10:PCBM shows excellent versatility for indoor and outdoor applications, low cost, and decent light stability, thus positioning itself as a strong candidate for multi-purpose laminated PV modules.^[23]

Experiments run on a domestic greenhouse in Sweden (latitude 58.4°N, 245° southwest, 40° tilt) from May to August 2022 in consecutive time slots of at least 45 days each. All modular configurations are fixed to the inner surface of the roof of the greenhouse (made of glass, thus adding additional light filtering and protection), and the connections are secured by tape. I - V tracing and data acquisition are performed autonomously by an Arduino UNO WiFi Rev2 setup featuring a wireless internet connection to the ThingSpeak™ cloud. The electronic circuit diagram of the I - V tracer is depicted in Figure 5c and consists of three main parts: i) an RC-filtering stage, ii) a voltage follower, and iii) a voltage amplifier (see Experimental Section). Exemplary I - V curves acquired indoors using this setup are shown in Figure S15, Supporting Information. Notably, the cost of the Arduino and the electronic parts required to build up to four (parallel) acquisition channels, temperature, and humidity sensors is below \$100 (in total), thus motivating its deployment onto further outdoor applications at a reasonably low cost.

Figure 5d shows the power (P) distribution extracted from a commercial silicon minimodule for a period of 1400 h, while mounted on the greenhouse. We observe the occurrence of sunny or cloudy (shadowing) moments distributed randomly

throughout the day as P data fluctuate strongly. On sunny days, both short-circuit current (I_{sc}) and P distributions appear very smooth (Figure S16, Supporting Information). Interestingly, data acquired on those same days suggests that OPV modules offer better light in-coupling than silicon as indicated by their broader normalized I_{sc} and P trends (Figure S16, Supporting Information). Figure 5e shows the P data for the silicon mini-module in a weekly polar format. Herein, each circular sector corresponds to the 24 h of a weekday, with the elapsed time running clockwise, and the radial axis corresponding to P . The color scale in Figure 5e matches that of Figure 5d, i.e., it corresponds to the elapsed time from 0 (red) to 1400 h (purple). Notably, the silicon minimodule appeared very stable in our experiments and it is used as a reference system when required,

e.g., using its (daily maximum) $I_{sc,max,day}$ as a probe of the daily irradiance (as a dedicated photodiode would do).

Figure 6 shows the results of our stability assays on selected module configurations and PALs, including weekly polar plots for P (Figure 6a,d,g); superimposed photocurrent images at the start and end of the experiments (Figure 6b,e,h); and normalized maximum daily power (P_{max}) data over a period of 45–60 days (Figure 6c,f,i). In this latter case, P_{max} data normalization occurs as follows: first, the maximum daily power value ($P_{max,day}$) is divided by $I_{sc,max,day}$, yielding P_{max} ; next, P_{max} is normalized by taking $P_{max}/P_{max,0}$, where $P_{max,0}$ refers to the P_{max} attained on the first day (i.e., day 0) of the outdoor stability experiment. Transmission spectra of archetypal laminated modules featuring different PALs, their AVT, and CGF values

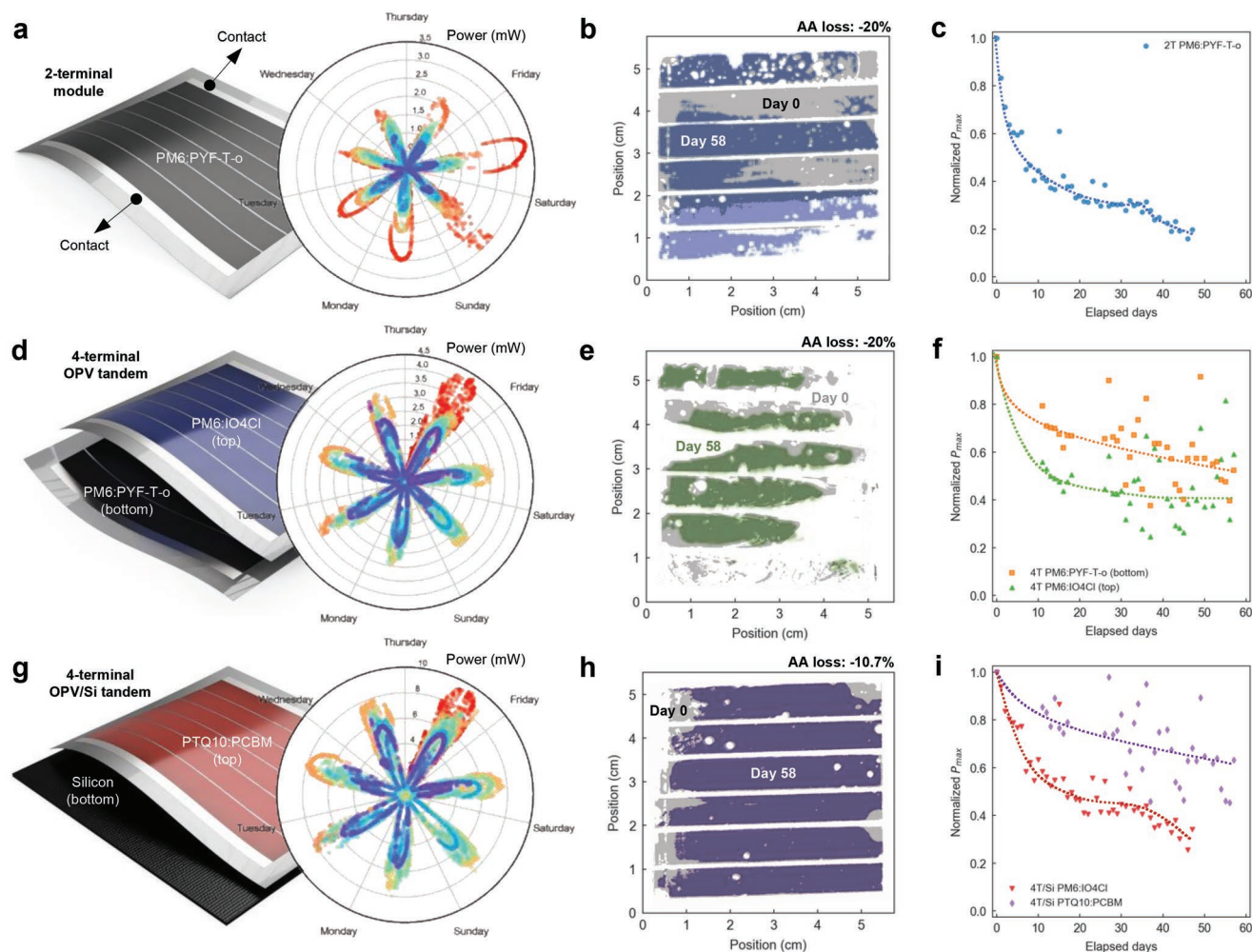


Figure 6. a) Weekly polar plot of P extracted from the 2-terminal standalone PM6:PYF-T-o module as a function of elapsed time (in color scale from red to purple). Module contacts are arranged in parallel to the coating direction. b) Photocurrent images of exemplary all-polymer modules at day 0 (gray and blue areas) and day 58 (blue areas only), marking the end of the experiment. In these modules, the AA is reduced by $\approx 20\%$ with respect to the initial value. c) Normalized P_{max} trend of the PM6:PYF-T-o module after correcting by $I_{sc,max,day}$. d) Weekly polar plot of P of the bottom PM6:PYF-T-o module in a 4-terminal configuration (with PM6:IO4Cl as top module). e) Photocurrent imaging of laminated PM6:IO4Cl modules revealing an AA loss of $\approx 20\%$ after 58 days on a greenhouse (the original area corresponds to gray and green colors; the aged area corresponds to green colors only). f) Normalized P_{max} trends of the OPV modules in a 4-terminal configuration: PM6:PYF-T-o (bottom module, orange squares) and PM6:IO4Cl (top module, green triangles). g) Weekly polar plot of P extracted from a PTQ10:PCBM module in a 4-terminal organic/inorganic tandem (with a silicon minimodule as bottom and opaque module). h) Photocurrent imaging of the PTQ10:PCBM module before (gray and purple areas) and after 58 days (purple area only) on the greenhouse indicating that AA loss increases up to 10.7%. i) Normalized P_{max} trends of two different organic/inorganic 4-terminal tandems: PTQ10:PCBM (purple diamonds) and PM6:IO4Cl (red triangles).

are included in Figure S17, Supporting Information. Figure 6a shows the weekly P data collected on a 2-terminal module using PM6:PYF-T-o as PAL. Herein, a severe device degradation occurs during the first week of the study, as evidenced by the shortened red “petals” that do not recover their original length (thus indicating irreversible degradation). Further analysis of the PV figures-of-merit reveals that the observed performance decay is mostly attributed to I_{sc} (Figure S18a, Supporting Information) and FF losses (Figure S18c,d, Supporting Information), as the V_{oc} (Figure S18b, Supporting Information) remains fairly stable (Figure S19a, Supporting Information) during the outdoor experiment. Interestingly, this degradation route is mostly absent during the thermal stability tests performed previously on smaller single devices while in the dark and in nitrogen. In that scenario, I_{sc} is far more stable and both V_{oc} and FF lead the observed performance drop; the reader is referred to Figure S19, Supporting Information, for a side-by-side comparison of the indoor and outdoor stability experiments. The corresponding photocurrent module images extracted on day 0 and on day 58 (end of the outdoor experiment, Figure 6b) indicate that delamination is a dominating degradation mode that promotes up to a 20% loss in the active area (AA, hence in I_{sc}). As a side effect, such a loss in AA could help to maintain high V_{oc} by keeping low dark currents (Figure S19a and Figure S20, Supporting Information). Therefore, in the transition to larger AA and outdoor testing conditions, additional degradation routes arise that could be attributed to several stressors absent in standard laboratory environments. These include heating/cooling cycles during the day that induce mechanical stress at the inorganic/organic interfaces (e.g., at the ETL/PAL interface or at the PET foil)^[38] or humidity and oxygen/water intake due to incomplete encapsulation.^[25]

Inspired by previous outdoor studies on perovskite minimodules,^[39] we perform an analysis of the ideality factor (n_{id}) of the PM6:PYF-T-o module (Figure S21b, Supporting Information). We do so by first checking that V_{oc} shows a weak dependence on temperature (Figure S21a, Supporting Information). We then group the data available during daylight time, at two different temperatures (25 ± 2 and 30 ± 2 °C) and in slots of 100 elapsed hours.^[39] The convex n_{id} trend observed (Figure S21b, Supporting Information) agrees well with the concave normalized P_{max} trend (Figure 6c), thus matching previous observations on perovskite minimodules tested outdoors. In that case, the convex/concave dichotomy between n_{id} and P_{max} is attributed to unsuccessful lamination allowing water intake. In OPV, water condensation is also known to be a significant stress factor affecting device lifetime.^[40] In a greenhouse, such degradation routes can be certainly amplified as temperature and humidity are found to vary between 10–55 °C and 20–90%, respectively, within periods of 24 h even at such high latitudes (Figure S22, Supporting Information).

Beyond standalone 2-terminal modules especially designed for agrivoltaics, Figure 6d schematically depicts the arrangement of two stacked OPV modules forming a 4-terminal tandem, including a bottom PM6:PYF-T-o module and a top PM6:IO4Cl module. Such device stack results in a “black” tandem with an AVT of 0.6% and a CGF of 3.1% (Figure S17c, Supporting Information), thus serving as a proof-of-concept for building integration beyond agrivoltaics, e.g., mostly opaque

facades or rooftops. Figure 6f indicates that, when protected in a 4-terminal configuration, the stability of the bottom PM6:PYF-T-o module improves (Figure 6f, orange squares) compared to the 2-terminal standalone module (Figure 6c). This fact suggests that a significant part of the losses in PM6:PYF-T-o modules are attributed to light exposure: in the 4-terminal configuration, the corresponding module is expected to receive a fraction of the irradiance (filtered by the top PM6:IO4Cl module) seen by the 2-terminal configuration. On the other hand, the top PM6:IO4Cl module degrades faster (Figure 6f, green triangles) than the bottom module (Figure 6f, orange squares) and suffers from similar delamination issues during the stability assay, namely, losing up to 20% of the original AA in a period of 58 days outdoors (Figure 6e). Notably, lamination of the PM6:IO4Cl module is technically more challenging than that of all-polymer blends as indicated by the smaller AA determined at the start of the experiment (Figure 6e).

Figure 6g depicts an organic/inorganic arrangement of a 4-terminal PV tandem, where an OPV module is used as top device and a silicon minimodule is employed as bottom device. In this experiment, two different high band gap OPV systems are employed, namely PTQ10:PCBM or PM6:IO4Cl, as top modules in combination with the inorganic counterpart. Among all PALs tested, the PTQ10:PCBM blend shows the best outdoor stability as indicated by the long multicolored petals in Figure 6g; comparative numerical data for all modules tested is shown in Table S1, Supporting Information. Moreover, delamination on this module is only half, compared to other PALs, reaching 10.7% at the end of our outdoor experiment (Figure 6h). We observe that delamination generally occurs at the coating edges of the module and far from the contact areas, thus indicating that device instabilities arise first along the coating (and encapsulation) directions in our setup. Notably, water ingress can find a preferential route precisely there and accelerate the device degradation,^[41] amplified by the hygroscopic nature of PEDOT(PSS). Improving the encapsulation methods in these areas could help in mitigating most delamination issues, which are so far omnipresent in all PALs and could *de facto* offer an improvement of 10–20% in the module lifetime (corresponding to the fractional loss in AA). On the other hand, the PM6:IO4Cl module in combination with the silicon minimodule follows a similar degradation pathway (Figure 6i, red triangles) compared to that in a 4-terminal OPV tandem configuration (Figure 6f, green triangles), during the first 30 days outdoors. This indicates that as both modules appear facing the sun first, they follow very similar degradation routes regardless of the type of module placed underneath. Therefore, the stability trend found for the PTQ10:PCBM module is expected to extrapolate well in a 2-terminal standalone configuration. Finally, we remark that the optical characteristics of laminated PTQ10:PCBM modules are competitive from an agrivoltaic perspective, with an AVT of 9.9% and a CGF of 25.6% (Figure S17d, Supporting Information).

3. Concluding Remarks and Outlooks

In this work, we first consider a low band gap polymer blend for its use as a light harvester in laminated PV devices and

modules. The all-polymer PM6:PYF-T-o blend shows adequate transmission properties (>30%) for plants (CGF) and humans (AVT) in small-area blade coated devices, which renders the blend attractive for agrivoltaic purposes. Despite their superior performance in terms of gh-FoM, unbalanced donor:acceptor ratios (1:4, w:w) are less stable than balanced counterparts (1:1.2, w:w) under standard thermal stability assays, thus promoting the up-scaling of the latter onto conceptual 25 cm² semitransparent and laminated modules. These are then mounted in a domestic greenhouse to reproduce realistic outdoor conditions as close as possible to their potential application niche. We monitor their performance for a period of up to 58 days by using an *I-V* tracer based on an Arduino motherboard that is connected wirelessly to the cloud. Beyond polymer blends, state-of-the-art NFA- and fullerene-based blends (PM6:IO4Cl and PTQ10:PCBM, respectively) are also included at this stage to compare degradation dynamics and failure modes between photoactive materials. An analysis of the P_{\max} decay and photocurrent images reveals that delamination is a common pitfall in these structures regardless of the type of device configuration (2- or 4-terminal tandems, in either organic/organic or organic/inorganic setups). Module delamination accounts for a 10 to 20% loss in AA and performance depending on the choice of PAL, with fullerene-based counterparts outperforming the remaining blends. Tracking of thermal and humidity data indicates that severe stress cycles naturally arise during day/night periods inside a greenhouse, thus contributing to accelerating the degradation pace of the agrivoltaic modules.

Among the laminated active layers tested in this work, we find that fullerene-based blends show better performance and stability than all-polymer and NFA-based counterparts, yet we acknowledge that our conclusions might be biased by a limited selection of screened materials and/or suboptimal processing conditions in air. Nevertheless, this indicates that within the OPV community, further work should be devoted to improving molecular stability when the materials (both PALs and interlayers) are casted under air-processing conditions.^[42] These are particularly challenging given the likelihood of deep trap^[43] and superoxide^[42,44] states to form in the PAL yet being the most industrially-relevant ones. Therefore, device stability is a key part of the greenhouse viability equation and ought to be included for improvement of the gh-FoM, c.f. the industrial figure-of-merit (i-FoM) was introduced to assess the industrial potential of OPV blends taking into consideration their PCE, synthetic complexity, and stability.^[29,45] On the other hand, our devices and modules include semitransparent PEDOT(PSS) electrodes, which impose limitations to charge transport under high irradiances (e.g., by limiting the FF below 30% during daylight time, Figure S18d, Supporting Information). Further research on scalable ITO-free, low-cost, flexible, and semitransparent structures is needed to incorporate more relevant contacts into the outdoor OPV market. Given the thermal stress imposed by the natural day-night cycles in a greenhouse, OPV modules should ideally leave oxides aside as contact interlayers due to their dissimilar thermal expansion coefficients. Their substitution by all-organic interlayers (likely based on polymers such as PEDOT^[46,47] or PNDIT-F3N)^[48] and the replacement of PET foils by polyimide^[38] might reduce the thermal expansion mismatch and improve device stability. Such mechanical stress

could be partly responsible for the observed module delamination, which constitutes a failure mode only found during our outdoor stability testing. This fact highlights the importance to perform field-testing studies in dedicated outdoor modules beyond standard laboratory assays and to include thermal and humidity cycling in testing protocols for agrivoltaic modules in the future. Finally, we suggest that further attention should be paid to improving encapsulation methods as their failure modes have been reportedly responsible for similar degradation dynamics as the ones observed in this work.^[39]

4. Experimental Section

Materials: The polymer donor PM6 (batch 261) and the polymer acceptor known as PYF-T-o^[17] (batch PA30) were purchased from eFlexPV. IO4Cl was obtained from Brilliant Matters (batch IOC03) and blended with PM6 from 1-Material (Lot# YY19116CH100). PTQ10 was purchased from Brilliant Matters (batch PQ1001) and PCBM was obtained from Solenne BV. Anhydrous solvents (*o*-xylene, chloroform, chlorobenzene), 1-chloronaphthalene, and diphenyl ether were purchased from Merck and used as received. ETL ink formulations were purchased from Avantama: N-10 (ZnO) for devices featuring evaporated back contacts and N-31 (SnO₂) for laminated devices and modules. For glass-supported devices, prepatterned ITO substrates (100 nm thick) were obtained from Ossila. 125- μ m-thick PET foils were obtained from Tekra (Melinex ST505). PEDOT(PSS) was obtained from Heraeus GmbH (Clevios PH1000). The monocrystalline silicon minimodules (0.5 W, 55 × 70 mm²) with a typical PCE of 17% and encapsulated with waterproof epoxy resin were purchased from Sseed Technology Co., Ltd.

Fabrication and Characterization of Laminated Devices and Modules: PEDOT(PSS) contacts were slot-die coated (Solar X3, FOM Technologies) using a high-conductivity formulation of PH1000, including ethylene glycol (EG) and a nonionic fluorosurfactant (Capstone FS-30 from Dupont) in the volume ratio 93.5:6:0.5 (PH1000:EG:FS-30), and the resulting ink further diluted in water (2:1, ink:water). PEDOT(PSS) patterns were dried at 130 °C. On the cathode side of small area devices, N-31 was spin coated at 2000 rpm in air for 30 s followed by annealing for 2 min at 115 °C. Following, PALs were deposited on both cathode and anode stacks by either spin coating at 2000 rpm (in air or in a nitrogen-filled glovebox), or by blade coating in air at 2.5 or 10 mm s⁻¹ depending on the desired film thickness. In blade coated devices, the anode side PAL was casted at 2.5 mm s⁻¹ in all cases. The blade coating temperature was adjusted to either 40 or 80 °C depending on the main solvent used (chloroform or *o*-xylene, respectively). PM6:PYF-T-o blends were prepared in two different ratios (1:1.2 and 1:4, w:w) in chloroform or *o*-xylene up to a total solid loading of 15 g L⁻¹, including in both cases 1 vol% of 1-chloronaphthalene (99:1, chloroform:1-chloronaphthalene or *o*-xylene:1-chloronaphthalene). Inks were stirred (300 rpm) for at least 2 h at room temperature and warmed up to 90 °C 30–45 min before their use. Following PAL deposition, both stacks were annealed for 5 min at 100 °C in air (or in the glovebox if the PALs were processed there) while in the dark (covered by a black box). The resulting stacks were laminated at the corresponding PAL interface at a temperature of 115 °C using a roll laminator (GSS DH-650S Graphical Solutions Scandinavia AB) while applying a force of ≈50 N (force sensor FlexiForce A201, Tekscan). Before lamination, the stacks were prepatterned with a scalpel to define the AA of the PV devices. Finally, two glass slides were used to confer mechanical strength to the laminated devices and silver paint was added to the exposed contact areas. These functional devices were characterized indoors and in air under an illuminance of 500 lux (calibrated with a Hamamatsu Si photodiode S1133-01) set by a cool LED source (emission as shown in Figure S6, Supporting Information, and collected with a QE-Pro (Ocean Optics) spectrometer). Their current-voltage characteristics were acquired using a Keithley 2400 source meter. The devices subjected to thermal stability testing (70 °C while in

the glovebox and in dark) were periodically measured in air after their thermalization.

In modular form factors, a laser-cut PET shim was attached to the blade applicator and aligned with the previously slot-die-coated PEDOT(PSS) contact lines. To achieve the correct thickness, N-31 was further diluted in 2-propanol (1:1, v:v). N-31 was blade coated in air at 5 mm s⁻¹ and 80 °C and further annealed for 3 min on the same coating stage (80 °C). Following, PALs were blade coated at 2.5 mm s⁻¹ and 80 °C for all blends employed. PM6 and PYF-T-o were blended in 1:1.2 (w:w) ratio up to a total concentration of 15 g L⁻¹ in *o*-xylene:1-chloronaphthalene (99:1, v:v); the corresponding films were annealed for 5 min at 100 °C in air. PM6 and IO4Cl were blended in 1:1.5 (w:w) ratio up to a total concentration of 15 g L⁻¹ in chlorobenzene as reported elsewhere;^[37] films were not further annealed in this case. PTQ10 and PCBM were blended in 1:1.5 (w:w) ratio up to a total concentration of 40 g L⁻¹ in *o*-xylene:diphenyl ether (85:15, v:v) as reported elsewhere;^[23] films were annealed for 2 min at 80 °C in air. Modules were completed by lamination in air at 115 °C and encapsulated with UV-curable epoxy resin. Photocurrent imaging was performed using an “economy LBIC” setup from infinityPV equipped with a 405 nm laser. Such wavelength allowed excitation of both donor and acceptor materials in all PALs employed.

Fabrication and Characterization of Devices with Evaporated Back Contacts: ITO substrates were subsequently cleaned and sonicated in acetone, Hellmanex 10 vol% solution in water, 2-propanol, and 10 vol% aqueous NaOH solution. N-10 was blade coated in air at 5 mm s⁻¹ and 40 °C, followed by annealing at 110 °C for 10 min before transferring to a nitrogen-filled glovebox. The PAL was blade coated in the glovebox in the form of a lateral thickness gradient, which is obtained by decelerating the applicator (typically from 90 to 5 mm s⁻¹) during film casting to form a combinatorial array of devices. PM6 and PYF-T-o were dissolved in *o*-xylene at the desired weight ratio (1:1 or 1:4), left stirring in the glovebox, and casted at 105 °C, followed by a 2 min drying step at 105 °C. MoO_x (50 nm) and Ag (120 nm) layers were finally evaporated in an ultra-high vacuum at a rate of 0.1 and 1 Å s⁻¹, respectively. The *J*-*V* characteristics of opaque devices were automatically acquired in air using a Keithley 2400 source meter in combination with an Arduino-based multiplexer/switcher to measure of up to 24 devices in a row. A SAN-EI Electric, XES-100S1 AAA solar simulator was used as an AM1.5G illumination source. The solar simulator was previously calibrated with a certified silicon solar cell (NREL).

Optical Modeling: Transfer matrix models for the calculated photocurrent were implemented in Python using NumPy^[49] and a dedicated open-source package (*tmm*).^[50] Normal incidence was assumed, and the integration extended from 360 to 950 nm under AM1.5G irradiance conditions. For the variable PAL, a Bruggeman's effective medium approximation was implemented to control the mixing of the complex-valued refractive index of the polymer blends, using those of the pristine materials as a reference.

Ellipsometry Measurements: Ellipsometry studies were performed on single polymer films deposited on glass substrates to determine film thickness and refractive index. Variable angle spectroscopic ellipsometry (VASE) data were recorded with a dual rotating compensator ellipsometer (J. A. Woollam, Co., Inc.) in the spectral range 170–1690 nm at angles of incidence in the range 45°–75° with step 10°. Modeling was performed using the software CompleteEASE (J. A. Woollam, Co., Inc.) whereby model-generated data were fitted to experimental data using non-linear regression. The refractive index of the glass substrate was determined on a sample without a polymer layer and then used for the polymer samples. For the polymer samples, a single-layer model (glass/polymer/ambient) was used with thickness and complex-valued refractive index $N = n + ik$ of the layer as fit parameters. Kramers-Kronig consistent B-splines^[51] were used as dispersion function for the index with restriction of positive imaginary part of the corresponding dielectric function $\epsilon = N^2$. The regression analysis provided 90% confidence intervals for the fit parameters which for the reported thickness values generally were 0.2 nm or smaller. More detailed models including surface roughness and thickness inhomogeneity grading were tested but did not

improve modeling significantly except for the PM6 film as described in Note S1, Supporting Information. For one blend sample (Figure S29, Supporting Information), an in-depth index profile was used.

Arduino I-V Tracer and Data Curation: The setup includes an Arduino UNO WiFi Rev2 motherboard and operational amplifiers (OpAmps) LM358P or LM358AN (Texas Instruments) that were powered with a TRACO POWER TMR 3-0522HI DC/DC converter sourced to the +5 V output pin of the Arduino. A sensor DS18B20 was used to track the temperature on the roof of the greenhouse. A dual temperature and humidity sensor DHT22 was used to track such variables inside the greenhouse. No special features apply to the remaining parts needed to complete the setup (i.e., resistors, capacitors, jumper wires, and breadboards).

According to the electronic circuit detailed in Figure 5c, the RC-filtering stage was used to smooth the pulse width modulation (PWM) signal of the Arduino, which was used as a voltage source during the *I*-*V* tracing routine. Then, an OpAmp in a voltage follower configuration served as a buffer, and alternatively, as an amplifier if required by the module features (i.e., if V_{oc} exceeds ≈ 5 V, which was the maximum output voltage provided by the Arduino motherboard). After proper connection to the solar cell, an additional OpAmp could be used to amplify the current (if required) before closing the circuit to one of the Arduino's analog input channels. The relevant figures-of-merit (I_{sc} , FF, V_{oc} , and P) were extracted from the corresponding *I*-*V* curves and wirelessly uploaded to the ThingSpeak™ cloud, featuring permanent real-time access for easy tracking worldwide. The process was repeated recursively every 30 s or 5 min depending on the experiment run, 24 h per day, for a period of up to 58 days in our work. In between consecutive acquisitions, the Arduino disconnects, and the devices remain in open-circuit conditions.

Before starting the data analysis, a curation of the raw data uploaded to the ThingSpeak™ cloud was performed by dropping anomalous values (namely, whenever FF exceeded 80% as the threshold). This was found to occur especially during the night hours (9 PM to 5 AM) due to instrumental noise and numerical errors in the extraction of the corresponding figure-of-merit (Figure S23, Supporting Information). During the day, data anomalies were detected mostly (and randomly distributed) in the silicon minimodules (Figure S23c, Supporting Information), which could be a result of partial cloud shadowing during the *I*-*V* curve acquisition (which takes between 20–30 s to complete) thus originating an anomalous reading.

Supporting Information

Supporting Information is available from the Wiley Online Library or from the author.

Acknowledgements

X.R.-M., S.R.-G., and O.I. acknowledge the Knut and Alice Wallenberg Foundation for funding. S.R.-G. is thankful to the Marie Skłodowska-Curie Actions (H2020-MSCA-IF-2020) for grant agreement No. 101025608, IDEAL. The authors acknowledge Dr. Bernhard Dörfling for building the electronic controller of the accelerated blade coater and Dr. M. Gibert-Roca for designing the corresponding multiplexor. M.C.-Q. thanks to the Spanish Ministry of Science and Innovation for funding through ISOSCELLES project (PID2021-128924OB-I00). The table of contents figure contains freely available resources from <https://flaticon.com>.

Conflict of Interest

O.I. is co-founder and co-owner of Epishine AB, a company producing and developing the use of OPV materials in indoor settings for energy supply under weak and artificial light.

Data Availability Statement

The data that support the findings of this study are available from the corresponding author upon reasonable request.

Keywords

agrivoltaics, building integrations, laminated solar cells, organic photovoltaics, outdoor stability

Received: December 2, 2022

Published online:

- [1] Ministerio de Agricultura, Alimentación y Medio Ambiente (MAAA), *Estadística Sobre Superficies y Producciones Anuales de Cultivos: Avance de Datos de Hortalizas*, Spanish Ministry of Agriculture, Food and Environment, Madrid, Spain **2021**, <https://www.mapa.gob.es/es/estadistica/temas/estadisticas-agrarias/agricultura/superficies-producciones-anualescultivos/>.
- [2] E. Ravishankar, R. E. Booth, J. A. Hollingsworth, H. Ade, H. Sederoff, J. F. DeCarolis, B. T. O'Connor, *Energy Environ. Sci.* **2022**, *15*, 1659.
- [3] E. Ravishankar, R. E. Booth, C. Saravitz, H. Sederoff, H. W. Ade, B. T. O'Connor, *Joule* **2020**, *4*, 490.
- [4] C. J. M. Emmott, J. A. Röhr, M. Campoy-Quiles, T. Kirchartz, A. Urbina, N. J. Ekins-Daukes, J. Nelson, *Energy Environ. Sci.* **2015**, *8*, 1317.
- [5] R. Meitzner, U. S. Schubert, H. Hoppe, *Adv. Energy Mater.* **2021**, *11*, 2002551.
- [6] A. Leon, K. N. Ishihara, *Resour Conserv Recycl* **2018**, *138*, 110.
- [7] G. A. dos Reis Benatto, M. Corazza, B. Roth, F. Schütte, M. Rengenstein, S. A. Gevorgyan, F. C. Krebs, *Energy Technol.* **2017**, *5*, 338.
- [8] S.-Y. Chang, P. Cheng, G. Li, Y. Yang, *Joule* **2018**, *2*, 1039.
- [9] C. S. Allardyce, C. Fankhauser, S. M. Zakeeruddin, M. Grätzel, P. J. Dyson, *Sol. Energy* **2017**, *155*, 517.
- [10] D. Wang, Y. Li, G. Zhou, E. Gu, R. Xia, B. Yan, J. Yao, H. Zhu, X. Lu, H.-L. Yip, H. Chen, C.-Z. Li, *Energy Environ. Sci.* **2022**, *15*, 2629.
- [11] E. Pascual-San José, A. Sánchez-Díaz, M. Stella, E. Martínez-Ferrero, M. I. Alonso, M. Campoy-Quiles, *Sci Technol Adv Mater* **2018**, *19*, 823.
- [12] J. Hou, O. Inganäs, R. H. Friend, F. Gao, *Nat. Mater.* **2018**, *17*, 119.
- [13] J. Yuan, Y. Zhang, L. Zhou, G. Zhang, H.-L. Yip, T.-K. Lau, X. Lu, C. Zhu, H. Peng, P. A. Johnson, M. Leclerc, Y. Cao, J. Ulanski, Y. Li, Y. Zou, *Joule* **2019**, *3*, 1140.
- [14] L. Liu, Y. Kan, K. Gao, J. Wang, M. Zhao, H. Chen, C. Zhao, T. Jiu, A.-Y. Jen, Y. Li, *Adv. Mater.* **2020**, *32*, 1907604.
- [15] D. Wang, H. Liu, Y. Li, G. Zhou, L. Zhan, H. Zhu, X. Lu, H. Chen, C.-Z. Li, *Joule* **2021**, *5*, 945.
- [16] H. Yu, S. Luo, R. Sun, I. Angunawela, Z. Qi, Z. Peng, W. Zhou, H. Han, R. Wei, M. Pan, A. M. H. Cheung, D. Zhao, J. Zhang, H. Ade, J. Min, H. Yan, *Adv. Funct. Mater.* **2021**, *31*, 2100791.
- [17] H. Yu, M. Pan, R. Sun, I. Angunawela, J. Zhang, Y. Li, Z. Qi, H. Han, X. Zou, W. Zhou, S. Chen, J. Y. L. Lai, S. Luo, Z. Luo, D. Zhao, X. Lu, H. Ade, F. Huang, J. Min, H. Yan, *Angew. Chem., Int. Ed.* **2021**, *60*, 10137.
- [18] H. K. Kim, H. Yu, M. Pan, X. Shi, H. Zhao, Z. Qi, W. Liu, W. Ma, H. Yan, S. Chen, *Adv. Sci.* **2022**, *9*, 2202223.
- [19] K. Hu, C. Zhu, K. Ding, S. Qin, W. Lai, J. Du, J. Zhang, Z. Wei, X. Li, Z. Zhang, L. Meng, H. Ade, Y. Li, *Energy Environ. Sci.* **2022**, *15*, 4157.
- [20] N. Schopp, G. Akhtanova, P. Panoy, A. Arbuz, S. Chae, A. Yi, H. J. Kim, V. Promarak, T. Nguyen, V. V. Brus, *Adv. Mater.* **2022**, *34*, 2203796.
- [21] N. Yao, J. Wang, Z. Chen, Q. Bian, Y. Xia, R. Zhang, J. Zhang, L. Qin, H. Zhu, Y. Zhang, F. Zhang, *J. Phys. Chem. Lett.* **2021**, *12*, 5039.
- [22] J. Bergqvist, T. Österberg, A. Melianas, L. E. Aguirre, Z. Tang, W. Cai, Z. Ma, M. Kemerink, D. Gedefaw, M. R. Andersson, O. Inganäs, *Npj Flex Electron* **2018**, *2*, 4.
- [23] X. Rodríguez-Martínez, S. Riera-Galindo, J. Cong, T. Österberg, M. Campoy-Quiles, O. Inganäs, *J. Mater. Chem. A* **2022**, *10*, 10768.
- [24] A. Ghaffari, Z. Saki, N. Taghavinia, M. M. Byranvand, M. Saliba, *Mater. Horiz.* **2022**, *9*, 2473.
- [25] Y. Zhang, I. D. W. Samuel, T. Wang, D. G. Lidzey, *Adv. Sci.* **2018**, *5*, 1800434.
- [26] M. O. Reese, S. A. Gevorgyan, M. Jørgensen, E. Bundgaard, S. R. Kurtz, D. S. Ginley, D. C. Olson, M. T. Lloyd, P. Morvillo, E. A. Katz, A. Elschner, O. Haillant, T. R. Currier, V. Shrotriya, M. Hermenau, M. Riede, K. R. Kirov, G. Trimmel, T. Rath, O. Inganäs, F. Zhang, M. Andersson, K. Tvingstedt, M. Lira-Cantu, D. Laird, C. McGuinness, S. (Jimmy) Gowrisanker, M. Pannone, M. Xiao, J. Hauch, et al., *Sol. Energy Mater. Sol. Cells* **2011**, *95*, 1253.
- [27] M. S. Vezie, S. Few, I. Meager, G. Pieridou, B. Döring, R. S. Ashraf, A. R. Goñi, H. Bronstein, I. McCulloch, S. C. Hayes, M. Campoy-Quiles, J. Nelson, *Nat. Mater.* **2016**, *15*, 746.
- [28] J. Yan, X. Rodríguez-Martínez, D. Pearce, H. Douglas, D. Bili, M. Azzouzi, F. Eisner, A. Virbule, E. Rezasoltani, V. Belova, B. Döring, S. Few, A. A. Szumska, X. Hou, G. Zhang, H.-L. Yip, M. Campoy-Quiles, J. Nelson, *Energy Environ. Sci.* **2022**, *15*, 2958.
- [29] W. Yang, W. Wang, Y. Wang, R. Sun, J. Guo, H. Li, M. Shi, J. Guo, Y. Wu, T. Wang, G. Lu, C. J. Brabec, Y. Li, J. Min, *Joule* **2021**, *5*, 1209.
- [30] M. C. Scharber, D. Mühlbacher, M. Koppe, P. Denk, C. Waldauf, A. J. Heeger, C. J. Brabec, *Adv. Mater.* **2006**, *18*, 789.
- [31] L. A. A. Pettersson, L. S. Roman, O. Inganäs, *J. Appl. Phys.* **1999**, *86*, 487.
- [32] X. Rodríguez-Martínez, E. Pascual-San-José, Z. Fei, M. Heeney, R. Guimerà, M. Campoy-Quiles, *Energy Environ. Sci.* **2021**, *14*, 986.
- [33] A. Armin, M. Velusamy, P. Wolfer, Y. Zhang, P. L. Burn, P. Meredith, A. Pivrikas, *ACS Photonics* **2014**, *1*, 173.
- [34] S. Nagasawa, E. Al-Naamani, A. Saeki, *J. Phys. Chem. Lett.* **2018**, *9*, 2639.
- [35] D. A. G. Bruggeman, *Ann. Phys.* **1935**, *416*, 636.
- [36] C. J. Traverse, R. Pandey, M. C. Barr, R. R. Lunt, *Nat. Energy* **2017**, *2*, 849.
- [37] Y. Cui, Y. Wang, J. Bergqvist, H. Yao, Y. Xu, B. Gao, C. Yang, S. Zhang, O. Inganäs, F. Gao, J. Hou, *Nat. Energy* **2019**, *4*, 768.
- [38] D. Koo, S. Jung, J. Seo, G. Jeong, Y. Choi, J. Lee, S. M. Lee, Y. Cho, M. Jeong, J. Lee, J. Oh, C. Yang, H. Park, *Joule* **2020**, *4*, 1021.
- [39] E. Velilla, F. Jaramillo, I. Mora-Seró, *Nat. Energy* **2021**, *6*, 54.
- [40] G. A. Soares, T. W. David, H. Anizelli, B. Miranda, J. Rodrigues, P. Lopes, J. Martins, T. Cunha, R. Vilaça, J. Kettle, D. Bagnis, *J. Renew. Sustain. Energy* **2020**, *12*, 063502.
- [41] T. S. Glen, N. W. Scarratt, H. Yi, A. Iraqi, T. Wang, J. Kingsley, A. R. Buckley, D. G. Lidzey, A. M. Donald, *Sol. Energy Mater. Sol. Cells* **2015**, *140*, 25.
- [42] J. Guo, Y. Wu, R. Sun, W. Wang, J. Guo, Q. Wu, X. Tang, C. Sun, Z. Luo, K. Chang, Z. Zhang, J. Yuan, T. Li, W. Tang, E. Zhou, Z. Xiao, L. Ding, Y. Zou, X. Zhan, C. Yang, Z. Li, C. J. Brabec, Y. Li, J. Min, *J. Mater. Chem. A* **2019**, *7*, 25088.
- [43] N. B. Kotadiya, A. Mondal, P. W. M. Blom, D. Andrienko, G.-J. A. H. Wetzelaer, *Nat. Mater.* **2019**, *18*, 1182.
- [44] E. M. Speller, A. J. Clarke, N. Aristidou, M. F. Wyatt, L. Francàs, G. Fish, H. Cha, H. K. H. Lee, J. Luke, A. Wadsworth, A. D. Evans,

- I. McCulloch, J.-S. Kim, S. A. Haque, J. R. Durrant, S. D. Dimitrov, W. C. Tsoi, Z. Li, *ACS Energy Lett.* **2019**, *4*, 846.
- [45] J. Min, Y. N. Luponosov, C. Cui, B. Kan, H. Chen, X. Wan, Y. Chen, S. A. Ponomarenko, Y. Li, C. J. Brabec, *Adv. Energy Mater.* **2017**, *7*, 1700465.
- [46] Y. Jiang, X. Dong, L. Sun, T. Liu, F. Qin, C. Xie, P. Jjiang, L. Hu, X. Lu, X. Zhou, W. Meng, N. Li, C. J. Brabec, Y. Zhou, *Nat. Energy* **2022**, *7*, 352.
- [47] T. Liu, L. Sun, X. Dong, Y. Jjiang, W. Wang, C. Xie, W. Zeng, Y. Liu, F. Qin, L. Hu, Y. Zhou, *Adv. Funct. Mater.* **2021**, *31*, 2107250.
- [48] K. Zhang, R. Xia, B. Fan, X. Liu, Z. Wang, S. Dong, H.-L. Yip, L. Ying, F. Huang, Y. Cao, *Adv. Mater.* **2018**, *30*, 1803166.
- [49] C. R. Harris, K. J. Millman, S. J. van der Walt, R. Gommers, P. Virtanen, D. Cournapeau, E. Wieser, J. Taylor, S. Berg, N. J. Smith, R. Kern, M. Picus, S. Hoyer, M. H. van Kerkwijk, M. Brett, A. Haldane, J. F. del Río, M. Wiebe, P. Peterson, P. Gérard-Marchant, K. Sheppard, T. Reddy, W. Weckesser, H. Abbasi, C. Gohlke, T. E. Oliphant, *Nature* **2020**, *585*, 357.
- [50] S. J. Byrnes, arXiv:1603.02720, v5, submitted: Dec **2020**.
- [51] B. Johs, J. S. Hale, *Status Solidi* **2008**, *205*, 715.